doi: 10.15407/ujpe62.04.0326

A.N. MOROZOVSKA,[1,2] M.D. GLINCHUK,[3] O.V. VARENYK,[1] A. UDOD,[3]
C.M. SCHERBAKOV,[2] S.V. KALININ[4]

[1] Institute of Physics, Nat. Acad. of Sci. of Ukraine
(46, Prosp. Nauky, Kyiv 03028, Ukraine)
[2] Taras Shevchenko Kiev National University, Physical Faculty, Chair of Theoretical Physics
(4e, Prosp. Academician Glushkov, Kyiv 03022, Ukraine)
[3] I. Frantsevich Institute for Problems of Materials Science, Nat. Acad. of Sci. of Ukraine
(3, Krizanovskogo Str., Kyiv 03142, Ukraine)
[4] Center for Nanophase Materials Sciences, Oak Ridge National Laboratory
(Oak Ridge, TN 37831)

FLEXOELECTRIC EFFECT IMPACT ON THE HYSTERETIC DYNAMICS OF THE LOCAL ELECTROMECHANICAL RESPONSE OF MIXED IONIC-ELECTRONIC CONDUCTORS

PACS 62.20.F-, 77.65.-j, 84.32.Ff

Strong coupling among electrochemical potentials, concentrations of electrons, ions, and strains mediated by the flexoelectric effect is a ubiquitous feature of moderate conductors, in particular, MIECs, the materials of choice in devices ranging from electroresistive and memristive elements to ion batteries and fuel cells. Corresponding mechanisms that govern bias-concentration-strain changes (Vegard expansion, deformation potential, and flexoelectric effect) are analyzed. Notably, that the contribution of the flexoelectric coupling to a local surface displacement of the moderate conductors is a complex dynamic effect which may lead to the drastic changing of the material mechanical response, depending on the values of flexoelectric coefficients and other external conditions. Numerical simulations have shown that the flexoelectric impact on the mechanical response ranges from the appearance of additional strain components, essential changes of a hysteresis loop shape and orientation, and the appearance of complex twisted hysteresis loops.

Keywords: flexoelectric effect, mixed ionic-electronic moderate conductors, thin films, nanoparticles, electrochemical strain microscopy.

1. Introduction

Mixed ionic-electronic moderate conductors (MIEC) such as solid electrolytes with rechargeable ions or vacancies, which also can be mobile, free electrons and/or holes, can display a reversible dynamics of the space charge layers that leads to a pronounced resistive switching between metastable states with high and low resistances [1–6] and unique dynamic properties (including hysteretic one) of the electro-mechanical response [7–14]. Though MIECs are promising candidates for the nonvolatile memory devices, the physical principles of the phenomena are yet not clear. In general, memristive systems cannot store energy, but they "remember" the total charge transfer due to the metastable changes of their conductance [15, 16]. Strukov *et al.* [17, 18] demonstrated that the memristive behaviour can be inherent to thin semiconductor films, when the drift-diffusion kinetic equations for electrons, holes, and mobile donors/acceptors are strongly coupled. In this case, the memory resistance depends on the thickness ratio of the doped and pure regions of a semiconductor. Note that the space charge dynamics in MIEC thin films were studied theoretically mostly in the framework of the linear drift-diffusion Poisson–Planck–Nernst theory and diluted species approximation [17–20].

One can expect a strong correlation between the electrophysical and electromechanical responses in MIECs [2]. Actually, the dynamic redistribution of the mobile species (ions, vacancies, and electrons)

concentrations caused by the electromigration (electric field-driven for charged species) and diffusion (concentration gradient-driven for both charged and neutral species) mechanisms can change the lattice molar volume [21]. The changes in the volume result in local electrochemical stresses, the so-called "Vegard stress" or "chemical pressure" [22, 23]. The Vegard mechanism plays a decisive role in the origin and evolution of local strains caused by the point defect kinetics in solids [24, 25].

Spatially confined and especially nanosized MIECs (such as thin films and nanoparticles) are intrinsically inhomogeneous in space and often possess inherent strains, chemical inhomogeneities, and/or polarization gradients, which are inevitably present near the surfaces, interfaces, and point and topological defects. According to experiments, as well as to phenomenological and microscopic theories, the flexoelectric effect [26–30], which can be spontaneous in nanosystems [31, 32], strongly influences the broad spectrum of their polar, electromechanical, electrochemical, and electrophysical responses [33–38].

2. Dynamics of Electromechanical Response in the Presence of Mobile Charged Impurity

In order to study the dynamics of the electrochemical strain microscopy (ESM) response, which appears, when the frequency of the *ac* voltage applied to a tip is higher or at least comparable with the inverse relaxation time of charge carriers, we need to consider kinetic equations for ionized impurity centers and electron fluxes. The problem becomes rather complex, if several factors, e.g. the impurity centers mobility and recharging rate are considered, mainly due to the appearance of hopping and generation terms in kinetic equations [39]. For the simplified analyses presented below, we will consider a situation where only mobile ionic defects and electrons are present in MIEC. We will assume that the hopping conduction and the ions recharging can be neglected. So, mobile defects remained fully ionized all the time.

Despite the evident oversimplifications of the model in comparison with physical reality, it can describe the main features of, e.g., the kinetics of protons or Li ions in solid electrolytes [7–14]. Actually, works [7–14] proposed analytical models of the *linearized* drift-diffusion kinetics in solid electrolytes with mixed electronic-ionic conductivity. These linear models, utilizing the decoupling approximation to solve the elastic problem and the diluted electrolyte approximation for mobile charge species, proved that the Vegard stresses can give rise to a local mechano-electrochemical response in Li-containing MIECs and quantum paraelectrics with oxygen vacancies.

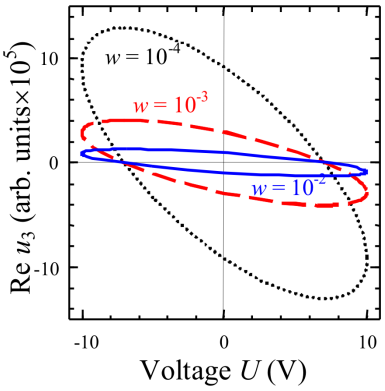

Fig. 1. Elliptic loops of the local ESM response calculated in the linear drift-diffusion theory for different dimensionless frequencies w (labels near the loops), (*Adapted with permission from* [8]). The dimensionless frequency $w = \omega\tau$, where ω is the applied frequency in s^{-1}, is the Maxwellian relaxation time of the space charge

It appears instructive to analyze the ESM dynamic response in terms of the hysteretic loop behavior, providing a direct link to the observables in the ESM experiment [9]. In the linear drift-diffusion regime, the complex quantities, namely the normal component of the surface displacement, $\tilde{u}_3(\omega, t) = u_3(0, \omega)\exp(i\omega t)$, and the *ac* voltage applied to a tip, $U_0(\omega, t) = U\exp(i\omega t)$, describe the elliptic loop in the complex plane. The parametric dependence of the observable quantity $\mathrm{Re}[u_3(\omega)\exp(i\omega t)]$ on $\mathrm{Re}[U(\omega)\exp(i\omega t)]$ describes the elliptic loop at a fixed frequency ω (see Fig. 1).

However, the analytical results of the linear drift-diffusion model are not applicable for MIEC film regions, where the electron accumulation and the strong accumulation of mobile defects are pronounced. As a result, the ESM loop shape is not elliptic, but pronounced hysteresis-like [9, 10]. Such regions usually originate near the film interfaces under the increase of an applied electric field to the values higher than the thermal activation field; the corresponding voltage is typically not more than several tens mV for ∼100-nm films. Naturally, the expected correlation between the electrophysical and electromechanical re-

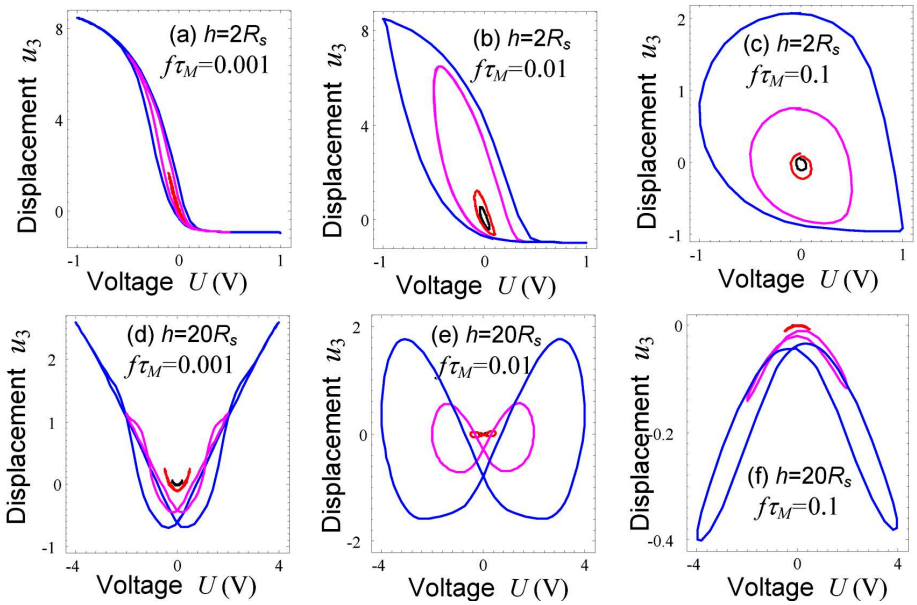

Fig. 2. Vertical component of the electromechanical response (displacement $\tilde{u}_3$) calculated for different frequencies: $\tau_M f$, film thickness h, asymmetric (a–c) and symmetric (d–f) boundary conditions. Maxwellian relaxation is τ_M, linear frequency $f = \omega/2\pi$, R_S is the screening radius. The film surface $z = 0$ is almost defect blocking, while the film surface $z = h$ is almost defect transparent (a–c). Both interfaces are defect blocking (d-f). (*Adapted from* [14])

sponses of MIEC films cannot be studied adequately within the linear drift-diffusion theory and the diluted electrolyte and decoupling approximations [12].

Appeared that the model, in which the concentration of mobile charged defects is restricted by the steric limit, predicts a great variety of dynamic electromechanical responses of MIEC films [10, 14]. In particular, the shape of local electromechanical response hysteresis loops demonstrates a crossover from the loops with pronounced memory window to butterfly-like loops depending on the boundary conditions and film thickness h (see Fig. 2). Different loops in Fig. 2 correspond to different values of maximal voltage U. At low frequencies $f\tau_M \leqslant 0.01$, the response curves are strongly asymmetric with respect to the voltage sign as anticipated from the asymmetry of the interfaces ionic conductivity. For the case, the total changes of the ionized defect amount contribute into the MIEC film surface displacement. The loops become noticeably open and almost symmetric with the frequency increase $f\tau_M \geqslant 0.01$. The inflation becomes much stronger with the thicknesses increase, and the loop shape becomes elliptic for small voltages $U < k_{\rm B}T/e$. For the high maximal voltage U, the loop shapes demonstrate a pronounced size effect: the transition from a slim hysteresis to the ellipse appears with the film thickness increase. The transition most probably originates from the electric field decrease with the film thickness increase: the thicker the film, the closer to linear is its response.

Some of the strain-voltage loop shapes shown in Fig. 2 can be, indeed, encountered in ionic semiconductors like correlated oxides, strontium titanate, and resistive switching materials. Consequently, the SPM measurements of the MIEC film surface displacement could provide important information about the local oxidation level, electron-phonon interactions via the deformation potential, and even Jahn–Teller distortions in films. Below, we concentrate on some examples with a special attention to the flexoelectric coupling.

3. Dynamics of ESM Response: Flexoelectric Effect Impact

To get insight into the mechanisms of local mechanic-electro-chemical response, in fact, the ESM image formation, we consider a cylindrical problem of the nonlinear drift-diffusion kinetics allowing for the Vegard mechanism, electrostriction flexoelectric effect, steric limit for the mobile ions concentration,

and Fermi–Dirac distribution function for the electron density, thus, including the most common form of a charge species nonlinearity inherent to the system. The finite-element modeling performed for the cylindrical geometry at different frequencies and bias voltage amplitudes provides the concentration and strain distributions registered by ESM microscopy [4].

A typical geometry of ESM microscopy with axially symmetric tip is shown in Fig. 3. All physical quantities depend only on the distances z from the tip-surface interface and the polar radius r (2D-problem). Mobile positively charged defects such as oxygen vacancies or impurity ions and free electrons are inherent to the film.

The mobile charge carriers redistribution creates the internal electric field, whose radial and normal components, $E_r = -\partial\varphi/\partial r$ and $E_z = -\partial\varphi/\partial z$, are determined from the Poisson equation for the electric potential φ written in the cylindrical coordinate frame:

$$\varepsilon_0\varepsilon\left(\frac{\partial^2\varphi}{\partial r^2}+\frac{1}{r}\frac{\partial\varphi}{\partial r}+\frac{\partial^2\varphi}{\partial z^2}\right)=-e\big(Z_dN_d^+(\varphi)-n(\varphi)\big). \quad (1)$$

Here, $\varepsilon_0 = 8.85\times10^{-12}$ F/m is the dielectric permittivity of vacuum; ε is a dielectric permittivity of MIEC, $e = 1.6\times10^{-19}$ C is the electron charge, electron density is n, positively charged defect concentration is N_d^+, and Z_d is their charge in the units of electron charge. For the particular case of the electroded film h in thickness, the electric potential satisfy fixed boundary conditions at the electrodes, $\varphi|_{z=0} = 0$, $\varphi|_{z=h} = U(r,t)$, $\varphi|_{r\to\infty} = 0$. The periodic voltage U is applied to the tip electrode. For demonstration, we use the Gaussian form, $U(r,t) = U_0\exp\left(-r^2/r_0^2\right)\sin(\omega t)$, and regard for that the tip lateral size r_0 is much smaller than the size of a computation cell.

The continuity equation for the mobile charged defect concentration N_d^+ is

$$\frac{\partial N_d^+}{\partial t}+\frac{1}{eZ_d}\left(\frac{1}{r}\frac{\partial(rJ_r^d)}{\partial r}+\frac{\partial J_z^d}{\partial z}\right)=G_d(N_d^+,n). \quad (2)$$

The defect current radial and normal components are proportional to the gradients of their electrochemical potentials ζ_d, namely $J_r^d = -eZ_d\eta_dN_d^+\left(\partial\zeta_d/\partial r\right)$ and $J_z^d = -eZ_d\eta_dN_d^+\left(\partial\zeta_d/\partial z\right)$, where η_d is the mobility coefficient that is regarded constant. The boundary conditions for the defect are blocking $J_d|_{z=0} = 0$; $J_d|_{z=h} = 0; J_d|_{r=R} = 0$. The function $G_d\left(N_d^+,n\right)\propto$ $\propto -\gamma_dN_d^+n+\gamma_T\left(N_d^0-N_d^+\right)$ describes the electron trapping by ionized defects and their generation by non-ionized ones. The function will be neglected in numerical simulations, primarily because its specific form and the values of trapping coefficients are typically unknown.

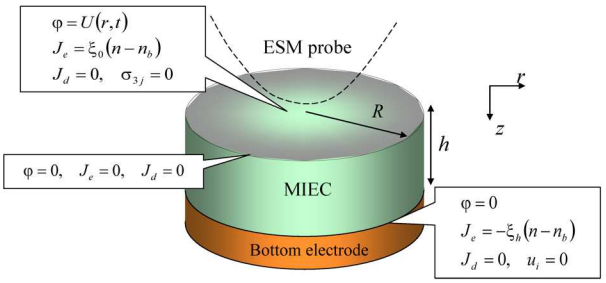

Fig. 3. Typical geometry for ESM microscopy. Definite electrical and mechanical boundary conditions are labeled. (*Adapted from [40]*)

The electrochemical potential level ζ_d is defined as

$$\zeta_d = -E_d - W_{ij}^d\sigma_{ij}+eZ_d\varphi+k_{\rm B}T\ln\left(\frac{N_d^+}{N_d^S-N_d^+}\right), \quad (3)$$

where E_d is the impurity level, the elastic stress tensor is σ_{ij}, T is the absolute temperature, $k_{\rm B}$ is the Boltzmann constant, and W_{ij}^d is the Vegard strain tensor. For the case of diagonal Vegard strain tensor, we have $W_{ij}^d\sigma_{ij}\equiv W\sigma$, where the first stress invariant is introduced as $\sigma = \sigma_{zz}+\sigma_{rr}+\sigma_{\varphi\varphi}$. The absolute values of W for ABO_3 compounds can be estimated from Refs. [41, 42] as $|W|\propto$ (1–50) Å^3. The maximal stoichiometric concentration of defects (N_d^S) in Eq. (3) involves steric effects [10]. For numerical estimates, one should assume that $N_d^S\equiv a^{-3}$, where a^3 is the minimal volume allowed per defect center. The steric effect limits the defect accumulation in a vicinity of the film surface. Actually, from Eq. (3), the concentration of defects is $N_d^+ = N_d^Sf\left(-E_d-W\sigma+eZ_d\varphi-\zeta_d\right)$, where $f(x) = (1+\exp(x/k_{\rm B}T))^{-1}$ is the Fermi–Dirac distribution function. Note that it is not clear whether the concentration of donor atoms N_d^0 and the maximal stoichiometric concentration of defects N_d^S (introduced here) should coincide. In fact, they should not.

The continuity equation for the electron current is as follows:

$$\frac{\partial n}{\partial t}-\frac{1}{e}\left(\frac{1}{r}\frac{\partial(rJ_r^e)}{\partial r}+\frac{\partial J_z^e}{\partial z}\right)=G_e(N_d^+,n). \quad (4)$$

The electron current components are $J_r^e = e\eta_e \times \times n\,(\partial\zeta_e/\partial r)$ and $J_z^e = e\eta_e n\,(\partial\zeta_e/\partial z)$, where η_e is the electron mobility coefficient, and ζ_e is the electrochemical potential. The function $G_e\left(N_d^+, n\right) = G_d\left(N_d^+, n\right) - n/\tau_n$ describes the electron trapping by an ionized defect and includes its finite lifetime. For the above-mentioned reasons, the function will be neglected in numerical simulations.

The boundary conditions for the electrons are taken in the linearized Chang–Jaffe [43] form, $(J_z^e - \xi_0(n-n_b))|_{z=0} = 0$, $(J_z^e + \xi_h(n-n_b))|_{z=h} = 0$, $J_e|_{r\to\infty} = 0$, where ξ_0 and ξ_h are positive rate constants related to the surface recombination velocity. The boundary conditions contain the continuous transition from the "open" electrodes ($\xi_{0,h} \to \infty$) to the interface limited kinetics ($0 < \xi_{0,h} < \infty$) and the "completely blocking" electrodes ($\xi_{0,h} = 0$).

Note that electrons are regarded sizeless, and the continuous approximation for their concentration in the conduction band is consistent with the following expression for electrochemical potential:

$$\zeta_e \approx E_{\rm C} - \Xi_{ij}\sigma_{ij} + k_{\rm B}T\,F_{1/2}^{-1}\left(\frac{n\,(\varphi)}{N_{\rm C}}\right) - e\varphi. \qquad (5)$$

The electrochemical potential ζ_e tends to the Fermi energy level $E_{\rm F}$ in equilibrium, $E_{\rm C}$ is the conductive band bottom, Ξ_{ij} is a deformation potential tensor also regarded diagonal for numerical estimates, $F_{1/2}^{-1}$ is the function inverse to the Fermi integral $F_{1/2}\,(\xi) = \frac{2}{\sqrt{\pi}}\int_0^\infty \frac{\sqrt{\zeta}d\zeta}{1+\exp(\zeta-\xi)}$; the effective density of states in the conductive band $N_{\rm C} = \left(\frac{m_n k_{\rm B}T}{2\pi\hbar^2}\right)^{3/2}$, and the electron effective mass is m_n. The electron density can be calculated from Eq. (5) as $n = N_{\rm C}F_{1/2}((e\varphi + \zeta_e - E_{\rm C} + \Xi\sigma)/k_{\rm B}T)$. The expression gives the thermodynamic distribution of the electron density under the condition $\zeta_e = -E_{\rm F}$.

Using the dependences of the concentrations of charged defects and electrons on the electrochemical potentials $\zeta_{d,e}$ derived directly from Eqs. (3) and (5), namely $N_d^+ = N_d^S f\,(-E_d - W\sigma + eZ_d\varphi - \zeta_d)$ and $n = N_{\rm C}F_{1/2}((e\varphi + \zeta_e - E_{\rm C})/k_{\rm B}T)$, one can express the potentials as the functions of mobile charged defects and electron chemical potentials $\mu_d = eZ_d\varphi - \zeta_d - W\sigma$ and $\mu_e = e\varphi + \zeta_e - \Xi\sigma$ in the following way: $N_d^+ = N_d^S f\,(\mu_d - E_d)$ and $n = N_{\rm C}F_{1/2}((\mu_e - E_{\rm C})/k_{\rm B}T)$. Then the continuity equations (2) and (4) become [40]

$$\frac{\partial f\,(\mu_d - E_d)}{\partial t} - \frac{1}{r}\frac{\partial}{\partial r}\left(r\frac{\partial F_d}{\partial r}\right) - \frac{\partial}{\partial z}\left(\frac{\partial F_d}{\partial z}\right) = 0, \quad (6a)$$

$$\frac{\partial}{\partial t}F_{1/2}\left(\frac{\mu_e - E_{\rm C}}{k_{\rm B}T}\right) - \frac{1}{r}\frac{\partial}{\partial r}\left(r\frac{\partial F_e}{\partial r}\right) - \frac{\partial}{\partial z}\left(\frac{\partial F_e}{\partial z}\right) = 0, \quad (6b)$$

where the functions $F_d = \eta_d f(\mu_d - E_d)(eZ_d\varphi - \mu_d - - W\sigma)$ and $F_e = \eta_e F_{1/2}\left(\frac{\mu_e - E_C}{k_{\rm B}T}\right)(\mu_e - e\varphi)$ are introduced.

The electrochemical strain can be calculated as follows. We used generalized Hooke's law Eq. (6) for a chemically active elastic solid media relating the concentration deviation from the average to the mechanical stress tensor σ_{ij} and elastic strain u_{ij}, where we suppose that only two kinds of species contribute to the elastic field and denote $W_{ij} \equiv W_{ij}^d$, $\Xi_{ij} \equiv \Xi_{ij}^C$.

Since the typical intrinsic resonance frequencies of the material are in the GHz range, well above the practically important limits both in terms of the ion dynamics and the AFM-based detection of localized mechanical vibrations, one can use the static equation of mechanical equilibrium, $\partial\sigma_{ij}/\partial x_j = 0$, for the modeling of mechanical phenomena (here, we neglected the first and second time derivatives). This leads to the equation for the mechanical displacement vector u_i in the film bulk:

$$c_{ijkl}\left(\frac{\partial^2 u_k}{\partial x_j \partial x_l} - W_{kl}\,\frac{\partial \delta N_d^+}{\partial x_j} - \Xi_{kl}\,\frac{\partial \delta n}{\partial x_j} - \right.$$
$$\left. - F_{klmn}\frac{\partial^2 P_m}{\partial x_j \partial x_n} - Q_{klmn}\frac{\partial\,(P_m P_n)}{\partial x_j}\right) = 0. \qquad (7)$$

Here, we introduced $\delta N_d^+\,(\mathbf{r}, t) = N_d^+\,(\mathbf{r}, t) - N_{d0}^+$ and $\delta n\,(\mathbf{r}, t) = n\,(\mathbf{r}, t) - n_e$, Q_{klmn} is the electrostriction tensor, and F_{klmn} is the flexoelectric effect tensor, and P_n is the electric polarization component that satisfies the corresponding (linear dielectric or nonlinear para- or ferroelectric) equation of state and boundary conditions, if the gradient term is included.

The boundary condition on the free surface $z = 0$ of the film is $\sigma_{3j}\,(z = 0, t) = 0$. The surface $z = h$ is clamped to a rigid substrate. Thus, $u_k|_{z=h} = 0$.

The hysteresis loops presented in Fig. 4 correspond to the deformation appearing in the ionic material under the action of an externally applied electrical field changing in time in a sinusoidal manner. Loops were computer-simulated on the base of the following assumptions: both electrodes are assumed to be blocking for donors and electrons; voltage is applied between the probe and the bottom electrode; verti-

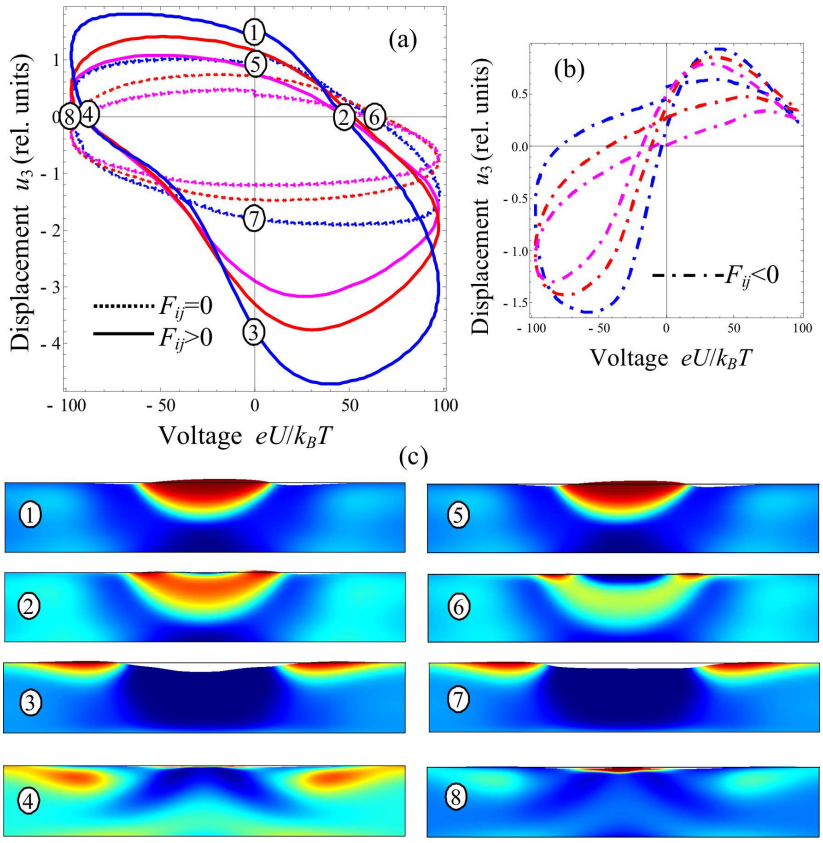

Fig. 4. (*a*), (*b*) Electromechanical response $\tilde{u}_3(V, f)$ calculated for different frequencies: (magenta: $\omega t_e = 0.157$, red: $\omega t_e = 0.104$ and blue: $\omega t_e = 0.052$) and zero (dashed curves), positive (solid curves) and negative (dash-dotted curves) flexoelectric coefficients. (*c*). The shape profile deviation from the empty rectangle shows the surface deformation

cal displacement of MIEC is measured directly under the probe. The different colors of the curves correspond to the different frequencies of the external field. Simulations are performed in the framework of the decoupling approximation, which means that the redistribution of charge carriers leads to the appearance of the local strain and displacement, while the strain itself does not affect the charge carrier distribution. Figure 4 illustrates the impact of the flexoelectric effect on the material mechanical response in the ESM response. The solid and dash-dotted curves correspond to the model involving the Vegard mechanism and the flexoelectric effect of different signs, while the dashed curves take only the Vegard mechanism into account. Note that the dashed and solid curves slightly change their orientation and become more asymmetric, as the frequency increases. A more detailed comparison of these curves shows that ones representing only the Vegard mechanism have an ellipsoid-like form with a center shifted relative to the origin (possibly explained by the non-equivalence of the characteristics of donors and electrons), while the solid curves have more complex and asymmetric shape, which is not ellipsoid-like, strictly speaking.

Additional information regarding the impact of the flexoelectric effect can be found from the series of the donor distribution profiles, Fig. 4, c, plotted for the different applied voltages during one period, i.e. different moments of time inside the period, indicated in Fig. 4, *a* by numbers 1–8.

In particular, contour maps 1–4 and 5–8 show the donors distribution and surface deformations at the different moments of time for positive and zero flexoelectric coefficients, correspondingly. For the sake of

clearness, only the actual area of the electromechanical response under the probe is shown. It can be concluded from the comparison of distributions 1 and 5 (as well as 3 and 7) that the flexoelectric effect causes a measurable additional strain. Since the inverse effect of the strain influence on the charge carriers distribution is neglected in the decoupling approximation, mapping pairs 1 and 5 (as well as 3 and 7) have the same donor redistribution and different surface displacements; pairs 2 and 6 (as well as 4 and 8) correspond to different donor distributions and strains. Maximal positive and negative surface strains correspond to the moments, when donors are highly localized or almost absent in the area under the probe. Zero strain occurs at the moments, when donors start moving inside or outside the area under the probe. The flexoelectric effect leads to the appearance of an additional delay in the carriers relaxation.

Complex effects take place with changing the sign of flexoelectric coefficients. The comparison of the curves in Fig. 4, *a* calculated for positive F_{ij} with the curves in Fig. 4, *b* calculated for negative ones shows that the curves have totally different forms. The loop has changed its orientation and no more has any similarity with elliptic shape. Another challenging effect is the twisting of the curves, which strongly depends on the frequency of the external field. Such a complex transformation of the behavior of curves with F_{ij} sign change can be probably explained in the terms of dynamic effects.

4. Summary Remarks

The performed analytical and numerical calculations show that the dynamic electromechanical response of the MIEC film is caused by the local changes of the concentration of mobile charged defects (ions or vacancies) (*conventional stoichiometry contribution*); concentration of free electrons (holes) (*electron-phonon coupling via the deformation potential*), and *flexoelectric effect*. Estimations performed for correlated oxides show that the strengths of all three contributions appeared comparable.

Note that the contribution of the flexoelectric coupling to the local surface displacement of moderate conductors is a complex dynamic effect, which may lead to an essential changing of the material mechanical response, depending on the values of flexoelectric coefficients and other external conditions. The numerical simulation has shown that the flexoelectric impact on the mechanical response may vary from the simple appearance of an additional deformation leading to relatively slight changes of the shape and orientation of a hysteresis loop up to the appearance of the complex twisting of hysteresis loops.

1. A. Sawa. Resistive switching in transition metal oxides. *Materials Today* **11**, 28 (2008) [DOI: 10.1016/S1369-7021(08)70119-6].
2. B. Magyari-Köpe, M. Tendulkar, S.-G. Park, H.D. Lee, Y. Nishi. Resistive switching mechanisms in random access memory devices incorporating transition metal oxides: TiO_2, NiO and $Pr_{0.7}Ca_{0.3}MnO_3$. *Nanotechnology* **22**, 254029 (2011) [DOI: 10.1088/0957-4484/22/25/254029].
3. D.-Sh. Shang, L. Shi, J.-R. Sun, B.-G. Shen. Local resistance switching at grain and grain boundary surfaces of polycrystalline tungsten oxide films. *Nanotechnology* **22**, 254008 (2011) [DOI: 10.1088/0957-4484/22/25/254008].
4. Y. Kim, S. Kelly, A. Morozovska, E.K. Rahani, E. Strelcov, E. Eliseev, S. Jesse, M. Biegalski, N. Balke, N. Benedek, D. Strukov, J. Aarts, I. Hwang, S. Oh, J.S. Choi, T. Choi, B.H. Park, V. Shenoy, P. Maksymovych, S. Kalinin. Mechanical control of electroresistive switching. *Nano Lett.* **13**, 4068 (2013) [DOI: 10.1021/nl401411r].
5. R. Waser, M. Aono. Nanoionics-based resistive switching memories. *Nature Mater.* **6**, 833 (2007) [DOI: 10.1038/nmat2023].
6. K. Szot, M. Rogala, W. Speier, Z. Klusek, A. Besmehn, R. Waser. TiO_2 – a prototypical memristive material. *Nanotechnology* **22**, 254001 (2011) [DOI: 10.1088/0957-4484/22/25/254001].
7. A.N. Morozovska, E.A. Eliseev, S.V. Kalinin. Electromechanical probing of ionic currents in energy storage materials. *Appl. Phys. Lett.* **96**, 222906 (2010) [DOI: 10.1063/1.3446838].
8. A.N. Morozovska, E.A. Eliseev, N. Balke, S.V. Kalinin. Local probing of ionic diffusion by electrochemical strain microscopy: Spatial resolution and signal formation mechanisms. *J. Appl. Phys.***108**, 053712 (2010) [DOI: 10.1063/1.3460637].
9. N. Balke, S. Jesse, A.N. Morozovska, E. Eliseev, D.W. Chung, Y. Kim, L. Adamczyk, R.E. Garcimatha, N. Dudney, S.V. Kalinin. Nanoscale mapping of ion diffusion in a lithium-ion battery cathode. *Nature Nanotechnol.* **5**, 749 (2010) [DOI: 10.1038/nnano.2010.174].
10. A.N. Morozovska, E.A. Eliseev, O.V. Varenyk, Y. Kim, E. Strelcov, A. Tselev, N.V. Morozovsky, S.V. Kalinin. Nonlinear space charge dynamics in mixed ionic-electronic conductors: Resistive switching and ferroelectric-like hysteresis of electromechanical response. *J. Appl. Phys.* **116**, 066808 (2014) [DOI: 10.1063/1.4891346].

11. A.N. Morozovska, E.A. Eliseev, A.K. Tagantsev, S.L. Bravina, L.-Q. Chen, S.V. Kalinin. Thermodynamics of electromechanically coupled mixed ionic-electronic conductors: Deformation potential, Vegard strains, and flexoelectric effect. *Phys. Rev.* B **83**, 195313 (2011) [DOI: 10.1103/PhysRevB.83.195313].
12. A.N. Morozovska, E.A. Eliseev, G.S. Svechnikov, S.V. Kalinin. Nanoscale electromechanics of paraelectric materials with mobile charges: Size effects and nonlinearity of electromechanical response of $SrTiO_3$ films. *Phys. Rev. B* **84**, 045402 (2011) [DOI: 10.1103/PhysRevB.84.045402].
13. A.N. Morozovska, E.A. Eliseev, S.V. Kalinin. Electrochemical strain microscopy with blocking electrodes: The role of electromigration and diffusion. *J. Appl. Phys.* **111**, 014114 (2012) [DOI: 10.1063/1.3675508].
14. A.N. Morozovska, E.A. Eliseev, S.L. Bravina, F. Ciucci, G.S. Svechnikov, L.-Q. Chen, S.V. Kalinin. Frequency dependent dynamical electromechanical response of mixed ionic-electronic conductors. *J. Appl. Phys.* **111**, 014107 (2012) [DOI: 10.1063/1.3673868].
15. L.O. Chua. Memristor – The missing circuit element. *IEEE Trans. Circuit Theory* **18**, 507 (1971) [DOI: 10.1109/TCT.1971.1083337].
16. L.O. Chua, S.M. Kang. Memristive devices and systems. *Proc. IEEE* **64**, 209 (1976) [DOI: 10.1109/PROC.1976.10092].
17. D.B. Strukov, G.S. Snider, D.R. Stewart, R.S. Williams. The missing memristor found. *Nature* **453**, 80 (2008) [DOI: 10.1038/nature06932].
18. D.B. Strukov, J.L. Borghetti, R.S. Williams. Coupled ionic and electronic transport model of thin-film semiconductor memristive behavior. *Small* **5** (9), 1058 (2009) [DOI: 10.1002/smll.200801323].
19. Y. Gil, O.M. Umurhan, I. Riess. Properties of solid state devices with mobile ionic defects. Part I: The effects of motion, space charge and contact potential in metal|semiconductor|metal devices. *Solid State Ionics* **178**, 1 (2007) [DOI: 10.1016/j.ssi.2006.10.024].
20. Y. Gil, O.M. Umurhan, I. Riess. Properties of a solid state device with mobile dopants: Analytic analysis for the thin film device. *J. Appl. Phys.* **104**, 084504 (2008) [DOI: 10.1063/1.2993618].
21. D. Seol, S. Park, O.V. Varenyk, S. Lee, Ho Nyung Lee, Anna N. Morozovska, Y. Kim. Determination of ferroelectric contributions to electromechanical response by frequency dependent piezoresponse force microscopy. *Scientific Reports* **6**, 30579 (2016) [DOI: 10.1038/srep30579].
22. S.M. Allen, J.W. Cahn. A microscopic theory for antiphase boundary motion and its application to antiphase domain coarsening. *Acta Metallurgica* **27** (6), 1085 (1979) [DOI: 10.1016/0001-6160(79)90196-2].
23. X. Zhang, W. Shyy, A. M. Sastry. Numerical simulation of intercalation-induced stress in Li-ion battery electrode particles. *J. Electrochem. Soc.* **154**, A910 (2007) [DOI: 10.1149/1.2759840].
24. M. Tang, H.Y. Huang, N. Meethong, Y.H. Kao, W.C. Carter, Y.M. Chiang. Model for the particle size, overpotential, and strain dependence of phase transition pathways in storage electrodes: Application to nanoscale olivines. *Chem. Mater.* **21** (8), 1557 (2009) [DOI: 10.1021/cm803172s].
25. M. Tang, W.C. Carter, J.F. Belak, Yet-Ming Chiang. Modeling the competing phase transition pathways in nanoscale olivine electrodes. *Electrochimica Acta* **56** (2), 969 (2010) [DOI: 10.1016/j.electacta.2010.09.027].
26. V.S. Mashkevich, K.B. Tolpygo. Electrical, optical and elastic properties of diamond type crystals. *Sov. Phys. JETP.* **5** (3), 435 (1957).
27. A.K. Tagantsev. Electric polarization in crystals and its response to thermal and elastic perturbations. *A Multinational Journal* **35** (3–4), 119 (1991) [DOI: 10.1080/01411599108213201].
28. S.M. Kogan. Piezoelectric effect during inhomogeneous deformation and acoustic scattering of carriers in crystals. *Sov. Phys. Solid State* **5** (10), 2069 (1964).
29. P.V. Yudin, A.K. Tagantsev. Fundamentals of flexoelectricity in solids. *Nanotechnology* **24** (43), 432001 (2013) [DOI: 10.1088/0957-4484/24/43/432001].
30. P. Zubko, G. Catalan, A.K. Tagantsev. Flexoelectric effect in solids. *Ann. Rev. Mater. Research* **43**, 387 (2013) [DOI: 10.1146/annurev-matsci-071312-121634].
31. E.A. Eliseev, A.N. Morozovska, M.D. Glinchuk, R. Blinc. Spontaneous flexoelectric/flexomagnetic effect in nanoferroics. *Phys. Rev. B* **79** (16), 165433 (2009) [DOI: 10.1103/PhysRevB.79.165433].
32. M.D. Glinchuk, E.A. Eliseev, A.N. Morozovska. Spontaneous flexoelectric effect in nanosystems (topical review). *Ferroelectrics* **500**, 90 (2016) [DOI: 10.1080/00150193.2016.1214994].
33. S.V. Kalinin, A.N. Morozovska. Multiferroics: Focusing light on flexoelectricity. *Nature Nanotechnology* **10**, 916 (2015) [DOI: 10.1038/nnano.2015.213].
34. D. Lee, A. Yoon, S.Y. Jang, J.G. Yoon, J.S. Chung, M. Kim, J.F.Scott, T.W. Noh. Giant flexoelectric effect in ferroelectric epitaxial thin films. *Phys. Rev. Lett.* **107** (5), 057602 (2011) [DOI: 10.1103/PhysRevLett.107.057602].
35. A.N. Morozovska, M.D. Glinchuk. Flexo-chemo effect in nanoferroics as a source of critical size disappearance at size-induced phase transitions. *J. Appl. Phys.* **119** (9), 094109 (2016) [DOI: 10.1063/1.4942859].
36. G. Catalan, B. Noheda, J. McAneney, L.J. Sinnamon, J.M. Gregg. Strain gradients in epitaxial ferroelectrics. *Phys. Rev. B* **72** (2), 020102 (2005) [DOI: 10.1103/PhysRevB.72.020102].
37. M.S. Majdoub, R. Maranganti, P. Sharma. Understanding the origins of the intrinsic dead layer effect in nanocapacitors. *Phys. Rev. B* **79** (11), 115412 (2009) [DOI: 10.1103/PhysRevB.79.115412].

38. A.N. Morozovska, E.A. Eliseev, Y.A. Genenko, I.S. Vorotiahin, M.V. Silibin, Y. Cao, Y. Kim, M.D. Glinchuk, S.V. Kalinin. Flexocoupling impact on size effects of piezoresponse and conductance in mixed-type ferroelectric semiconductors under applied pressure. *Phys. Rev. B* **94**, 174101 (2016) [DOI: 10.1103/PhysRevB.94.174101].
39. Y. Gil, Y. Tsur, O.M. Umurhan, I. Riess. Properties of solid state devices with significant impurity hopping conduction. *J. Phys. D: Appl. Phys.* **41**, 135106 (2008) [DOI: 10.1088/0022-3727/41/13/135106].
40. O.V. Varenyk, M.V Silibin, D.A Kiselev, E.A. Eliseev, S.V. Kalinin, A.N. Morozovska. Self-consistent modelling of electrochemical strain microscopy in mixed ionic-electronic conductors: Nonlinear and dynamic regimes. *J. Appl. Phys.* **118**, 072015 (2015) [DOI: 10.1063/1.4927815].
41. D.A. Freedman, D. Roundy, T.A. Arias. Elastic effects of vacancies in strontium titanate: Short- and long-range strain fields, elastic dipole tensors, and chemical strain. *Phys. Rev.* B **80**, 064108 (2009) [DOI: 10.1103/PhysRevB.80.064108].
42. X. Zhang, A.M. Sastry, W. Shyy. Intercalation-induced stress and heat generation within single lithium-ion battery cathode particles. *J. Electrochem. Soc.* **155**, A542 (2008) [DOI: 10.1149/1.2926617].
43. H.-Ch. Chang, G. Jaffe. Polarization in electrolytic solutions. Part I. Theory. *J. Chem. Phys.* **20**, 1071 (1952) [DOI: 10.1063/1.1700669].

Received 30.11.16

Г.М. Морозовська, М.Д. Глинчук,
О.В. Вареник, О. Удод, К.М. Щербаков, С.В. Калінін

ВПЛИВ ФЛЕКСОЕЛЕКРИЧНОГО ЕФЕКТУ НА ГІСТЕРЕЗИСНУ ДИНАМІКУ ЛОКАЛЬНОГО ЕЛЕКТРОМЕХАНІЧНОГО ВІДГУКУ НАПІВПРОВІДНИКІВ З ІОННО-ЕЛЕКТРОННОЮ ПРОВІДНІСТЮ

Р е з ю м е

Сильний зв'язок між електрохімічними потенціалами, концентрацією електронів, іонів і деформацій, зпричинених флексоефектом є поширеною ознакою напівпровідників з іонно-електронною провідністю – матеріалів, які вибирають для пристроїв, починаючи від елементів опору та пам'яті і до іонних батарей і паливних елементів. В статті аналізуються відповідні механізми, які регулюють зміни концентра та зміщення (розширення Вегарда, деформаційний потенціал і флексоефект). Цікаво, що внесок флексоелектричного зв'язку в локальне зміщення поверхні напівпровідників є складним і динамічним ефектом, який може призвести до різкої зміни механічного відгуку, залежно від значень флексоелектричних коефіцієнтів і інших зовнішніх умов. Чисельне моделювання показало, що вплив флексоелектричного ефекту на механічний відгук може змінюватися від простого, до появи додаткової деформації, що призводить до порівняно невеликої зміни форми петлі гістерезису і зміни орієнтації, і до появи складних скручених петель гістерезису.